Journal of Magnetic Resonance 304 (2019) 42–52

Contents lists available at ScienceDirect

Journal of Magnetic Resonance

journal homepage: www.elsevier.com/locate/jmr

Development of an L-band rapid scan EPR digital console

Hideo Sato-Akaba [a,*], Mark Tseytlin [b]

[a] Department of Systems Innovation, Graduate School of Engineering Science, Osaka University, Toyonaka, Osaka 560-8531, Japan
[b] Department of Biochemistry, School of Medicine, West Virginia University, Morgantown, WV, USA

ARTICLE INFO

Article history:
Received 29 March 2019
Revised 9 May 2019
Accepted 10 May 2019
Available online 10 May 2019

Keywords:
Rapid scan EPR
Direct RF band-pass subsampling
Reflection reduction control
In-vivo applications
FPGA

ABSTRACT

The development of a digital console for *in-vivo* rapid scan electron paramagnetic resonance (RS-EPR) spectroscopy and imaging is described in detail. The console was build using field programmable gate array (FGPA) technology that permits real-time control of the resonator and scanning magnetic fields during the measurements. Automatic resonator tuning and matching are achieved by implementing a digital feedback control system and using voltage-tunable capacitors. A band-pass subsampling method is used to directly digitize EPR signals at the carrier frequencies of about 1.2 GHz. The magnetic field scan waveforms, excitation EPR frequency, and sampling clock are all internally synchronized. Full-cycle RS-EPR signals are accumulated in the FPGA in real time without any time gaps. The result is the elimination of the re-arm time, during which data are not acquired. The proposed design in this manuscript has a small footprint and is relatively low cost. The FPGA-based RS-EPR system was tested using standard LiNc-BuO and tempone-d16 samples. The RS-EPR linewidth of the LiNc-BuO sample was consistent with an independent pulsed EPR measurement.

1. Introduction

Direct RF sampling of continuous wave electron spin resonance (CW-EPR) signals has been implemented in several laboratories worldwide [1–7]. Increase in speed and decrease of aperture jitter of analog-to-digital converts (ADC) enabled direct digitization and real-time averaging of radiofrequency (RF) and microwave signals. The use of band-pass subsampling [8], which enables detection of the RF signals from a resonator at a lower sampling rate than the Nyquist rate, has been demonstrated in *in-vivo* EPR imaging with the help of field programmable gate array (FPGA) technology [7,9,10]. Direct signal digitization has multiple advantages, including a reduction in the number of RF components compared to conventional homodyne detection and flexibility in signal processing with a reconfigurable FPGA IC without changing hardware components. The result is lower system cost and noise reduction. A disadvantage of this digital detection method is that it is sensitive to small detuning deviations from the critical coupling of the resonator. A low-power reflection from the resonator combined with a leakage signal from the RF excitation may saturate a first stage low noise amplifier (LNA). The amplified output voltage may also exceed the ADC input range. To overcome this problem, the FPGA-based automatic reflection reduction control has been implemented. It uses a digital feedback loop in which the down-converted reflection signal is integrated and negatively applied to the tuning and matching capacitors to achieve approximately critical coupling of the resonator. The implemented reduction of the RF reflection signal from the resonator and leakage signal from the RF excitation fed to a receiver circuit permitted achieving 100 dB excitation/reception isolation, which is considerably better compared to 20–25 dB isolation of a typical circulator [7].

With the goal to evaluate the performance of the digital detection method for rapid scan (RS) EPR [11–14], a previously developed FPGA-based design was modified. The original EPR imaging system operated as a standard continuous-wave (CW) modality using a reflection resonator [7]. The modifications included the development of a feedback system that controls phase and amplitude of the magnetic field scans (critically important for RS-EPR deconvolution [15]), background cancelling, and a new matching and tuning circuitry that works within a wide range of frequencies and resonator loads.

The use of the reflection resonator has been shown to have disadvantages for RS-EPR in comparison with the bi-modal transmission resonator, especially at low frequencies [16]. A bimodal resonator was used for *in-vivo* RS-EPR imaging at 250 MHz frequency [17]. The advantage of the bimodal resonator is that the phase noise of the RF excitation source is attenuated. This advantage is more pronounced at lower frequencies (250 MHz) and less at higher frequencies (X-band and higher) because the resonator

* Corresponding author.
E-mail address: akaba@ee.es.osaka-u.ac.jp (H. Sato-Akaba).

https://doi.org/10.1016/j.jmr.2019.05.003
1090-7807/

bandwidth increases with the frequency. The use of the reflection resonator is more advantageous in the L-band compared to 250 MHz. Bi-modal designs are substantially more difficult to build and in particular to operate. Five parameters need to be controlled for two sub-resonators: two tuning and matching of the resonators, and isolation between the resonators. Maintaining the latter is critical for the resonator performance, especially in *in-vivo* experiments. Animal motion modulates not only tuning and matching of individual excitation and detection resonators, but also the isolation. The present work demonstrated that the reflection reduction control can be used to maintain up to 100 dB of isolation in real time. This isolation is higher than previously reported 56 and 35 dB values for the unloaded and mouse-loaded bimodal resonator, respectively [18].

The developed RS-EPR console is controlled by a locally-developed LabVIEW software. A LabVIEW function to perform RS-EPR deconvolution algorithm was written and integrated into the software. The algorithm transforms transient time-domain signals into absorption EPR spectra [15]. A LiNc-BuO spin probe [19,20] and tempone-d16 were used to evaluate the developed digital system. Due to the fact that RS-EPR uses broadband quadrature detection, the developed RF bridge (with minimum modifications described below) permits pulsed EPR experiments.

2. Method

2.1. RS and pulsed EPR system

2.1.1. Magnet and RS scan coils

Fig. 1 shows a block diagram of the RS and pulsed EPR spectrometer/imager that has been developed. A permanent magnet (MR-PMAG05, Sumitomo Special Metals Co., Ltd, Japan) was used for testing of the RS-EPR digital console at 1.2 GHz. The static field strength of the magnet is about 43 mT at room temperature. The magnetic field can be varied using additional coils installed on the magnet. The coils are driven by a current source constructed locally using an op-amp IC (OPA549, Texas Instruments, Inc., USA) supplied with ±24 V. The sinusoidal scanning magnetic field required for RS experiments was generated by a Helmholtz pair of coils (radius 70 mm, inductance 2.28 mH, coil constant 0.65 mT/A). The coils were resonated using a bank of capacitors. Scans with a maximum width of 3 mT at 15 kHz and 33 kHz were generated by the operational amplifier that uses ±28 V power supplies. This voltage defines the maximum scan width.

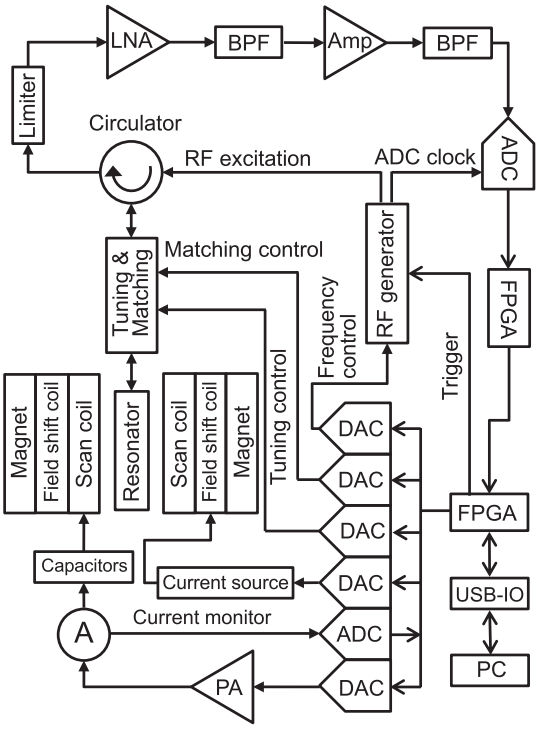

Fig. 1. Schematic diagram of the L-band rapid scan and pulsed EPR system.

2.1.2. RS and pulsed EPR digital console

The major components of the RS and pulsed EPR digital console were an RF acquisition circuit, an RF generator circuit, and a DSP & control circuit. The RF acquisition circuit consisted mainly of a high-speed 500 MSPS 12-bit ADC IC (AD9434, Analog Devices Inc., USA) and an FPGA IC (Cyclone VE, Intel Corp., USA). Digitized data from the ADC was sent to the FPGA. The data was then processed in the FPGA to generate serial signals that were fed to the DSP & control circuit. The RF generator circuit has one input port for a frequency tuning control signal and two output ports for ADC clock and RF excitation signals. Details of the RF generator circuit were described in the next section. The frequency tuning control signal was fed from the DSP & control circuit. Two RF signals with different frequencies were generated; one of them was fed to the resonator and the other was fed to the ADC IC as a sampling clock signal.

The DSP & control circuit consisted mainly of an FPGA (Cyclone VE), a DC-DC converter (LT1935, Analog Devices Inc.) used to generate ±12 V and +24 V, five digital-to-analog converters (DACs) (DAC8811, Texas Instruments Inc.) and a USB IO IC (FT2232H, FTDI Ltd., UK). The offset drift of the DAC output due to temperature was observed during the warming up of the system. However, this drift was lower than 1 mV, which is negligible compared with the DAC output range. For changing the static field, one of the DAC outputs was fed to the current source to drive the coils in the main magnet. The amplitude coefficients were updated at every accumulated scan to change the field shift. For the field scan, a digital sinusoidal signal was generated with a numerically controlled oscillator (NCO) in the FPGA and then converted to the analog signal using the DAC IC. This converted signal was fed to the power amplifier that drives the field scan coil via a current sensor (ACS70331, Allegro MicroSystems, LLC, USA). The output of the sensor was digitized by a 14-bit serial ADC (LTC2314-14, Analog Devices Inc.) which was controlled from the DSP & control circuit. For reflection reduction control, two digital control signals were generated in the FPGA and then converted to analog signals with two DAC ICs. Data acquisition and sending parameters to the FPGA were controlled by a LabVIEW-based program through a USB port on macOS 10.13.6.

2.1.3. RF generator circuit

Two types of RF circuits were designed for generation of the ADC clock and RF excitation signals. Those frequencies were controlled by the analog control signal from the DSP & control circuit. The detailed circuits were shown in Fig. 2. The first one was a prescaler-based RF generator which consisted of a voltage-controlled oscillator (VCO) (HMC1162, Analog Devices Inc.), two different prescaler ICs (HMC705, HMC905, Analog Devices Inc.), and gain block amplifiers (HMC482, HMC452, Analog Devices Inc.). The frequency division factors for HMC705 and HMC905 were 11 and 4, respectively. The output power was about 27 dBm for the CW excitation. The final power at the input port of the circulator varied with a variable attenuator (50DR-046, JFW Industries, Inc., USA). The second one was a direct digital synthesis (DDS)-based RF generator which consisted of a VCO (CVCO55CC-3200-3200, Crystek Corp., USA), two 3.5 GSPS DDS ICs (AD9914, Analog Devices Inc.), two FPGA ICs (Cyclone VE), RF gain block

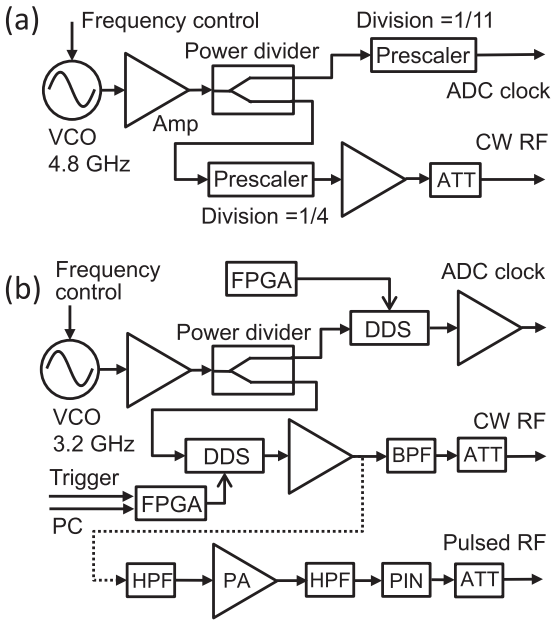

Fig. 2. Schematic diagram of the RF generator circuits based on the prescaler (a) and direct digital synthesis (b). ADC clock and RF excitation signals were generated from a single VCO to make synchronous detection.

amplifiers (HMC482), and a final stage power amplifier (HMC8500, Analog Devices Inc.). The parameter pins of the DDS IC were connected to the FPGA IC controlled by the PC. The DDS clock signal fed from the VCO was around 3.2 GHz, so that the maximum sinusoidal output frequency became 1.28 GHz. The reason to choose the DDS IC instead of the prescaler IC was that RF amplitude, phase, and frequency can be separately programed from the PC so that it can be used for pulsed and CW mode. However, the phase noise and noise floor in the DDS-based generator is often higher than those in the prescaler-based generator from the performance of the RF ICs shown in the datasheets. The update frequency for DDS settings is around 133 MHz = DDS clock frequency/24, so that the resolution of the pulse width should be around 7.5 ns. The maximum output power from the final stage amplifier was around 39.5 dBm (9 W). Two PIN diodes (CLA4607, Skyworks Solutions Inc., USA) in series and high pass filter (CHPFL-1000, Crystek Corp.) inserted between the amplifier and the circulator were used to reject noise of the RF generator during the reception, that decreased the output power to around 35 dBm (3 W).

2.1.4. Analog front-end for data acquisition

The RF reflection bridge consisted of an RF circulator (MAFR-000645, Skyworks Solutions Inc.) and a single loop-gap resonator. The RF signal from the resonator was fed from a circulator to a low-noise amplifier IC (LNA) (SKY67153-396LF, Skyworks Solutions Inc.) via an RF limiter PIN diode (CLA4605, Skyworks Solutions Inc.). The insertion loss of the circulator and the PIN diode was 0.5 dB and 0.1 dB from the manufacturer datasheets, respectively. The amplified signal was filtered with a band-pass filter (BPF) (ZX75BP-1205+, Mini-Circuits, USA) and then fed to a post-amplifier consisted of two LNA ICs (SKY67153-396LF and QPA7489, Qorvo, USA). An additional BPF (ZX75BP-1205+) was inserted before digitizing a signal at the ADC. The total gains of the whole amplifying stage including the circulator, cables, and connectors were 61 dB at 1.2 GHz. The noise figure (NF) was less than 2 dB including insertion losses of the circulator and the limiter PIN diode.

2.1.5. Current sensor circuit

Scan amplitude and phase are the inputs for the RS-EPR deconvolution algorithm. Stability and accurate assessment of these parameters in experiments are important in order to avoid distortion of the deconvolved spectra. The magnetic field generated by the scan coils is proportional to the current in the coils. Measurement of this current using the circuit shown in Fig. 3 permits accurate field control. In this circuit, two GMR-based current sensor ICs (ACS70331) are connected in reverse direction to give differential output signals which are fed to separate buffer amplifiers (LT6200, Analog Devices Inc.), which followed by an active low pass filter (LT6600-2.5, Analog Devices Inc.). The output signal was digitalized using the serial ADC in the console.

2.1.6. Resonator with tuning and matching circuit

Implementation of the direct detection at the carrier frequency requires the use of high gain (60 dB or higher) amplification. As a result, even low-power non-EPR RF signal contributions may overwhelm both the amplifier and the ADC in the detection system. The automatic reflection reduction control is a critical component of our design that ensures reliable detection of EPR signals. For the purpose of tuning and matching, voltage-controlled capacitors such as varactor diodes are often used. Several types of tuning and matching circuits have been reported [21–24]. Recently, a new type of RF tunable capacitor PTIC (passive tunable integrated capacitor) that uses the tunable dielectric properties of barium strontium titanate (BST) is commercially available (STPTIC, STMicroelectronics, Switzerland). This product was developed for wireless communication RF systems operating in the range from 700 MHz to 2.7 GHz. Maximum CW rating power is 40 dBm (10 W), which is within the specification range of CW and RS-EPR spectrometers. Therefore, in the present work, PTICs were used instead of varactor diodes.

Fig. 4 shows the electric circuit used for a resonator with tuning and matching controls. The major factors that determinate the resonant frequency are the resonator loop inductance L4 and the parallel capacitor C3 that was made using a short semi-rigid cable (see Fig. 4c). Series capacitors C2 and C4, which have equal capacitance, serve the purpose to decrease the resonance frequency and the impedance generated from L4 and C3. A PTIC C_T, which varies the net series capacitance, is used to electrically control the resonant frequency. To broaden the tunable frequency band, an inductor L3 was added in parallel with C_T. The inductive reactance of the L3 can subtract the reactance of C_T with same amount while C_T varies, which increase ratio of the reactance change due to the bias voltage. Inductors L1 and L2 and a PTIC C_M were used for the resonator matching control. The values of L1 and L2 were selected based on the loaded loop impedance and operating RF frequency (See Table 1). The bias voltage induced to the C_M can change the impedance of the resonator. Addition of the parallel inductor L2

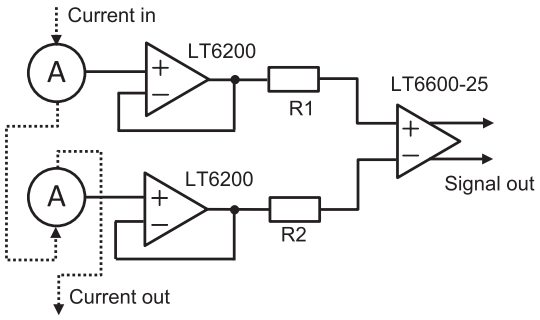

Fig. 3. Schematic diagram of the current sensor circuit to measure the current fed to the field scan coil.

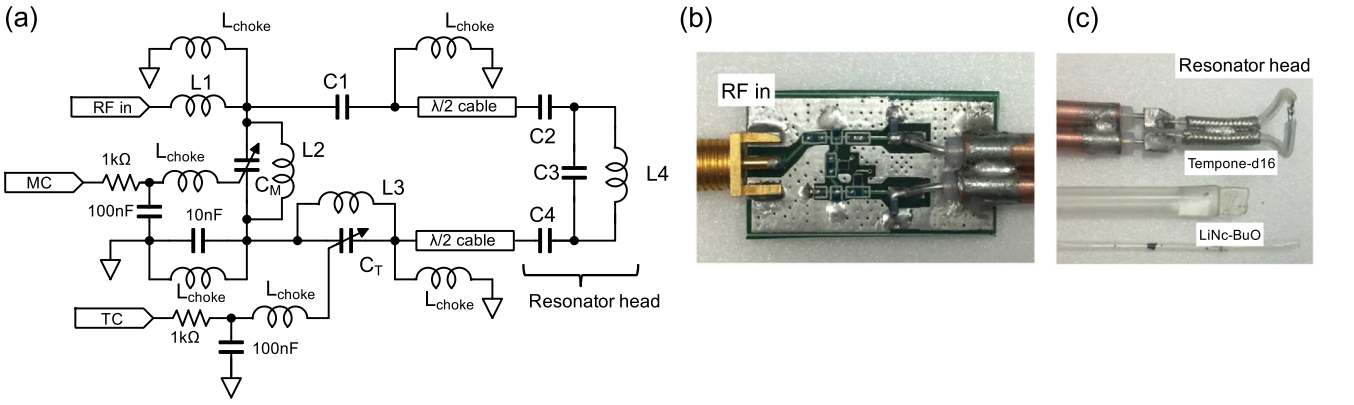

Fig. 4. Schematic diagram of the tuning and matching circuit (a), photograph of the printed circuit board (b) and the resonator head (c). The samples used for this work were also shown in (c). Two PTICs C_T and C_M were used for reflection reduction control. Matching control (MC) and tuning control (TC) signals were fed from the console. The RF input port was connected to the circulator with a SMA cable. The bias circuits for the PTICs were located at other side of the PCB.

Table 1
The values for capacitors and inductors used for the resonator. The sizes of the chip components were also shown.

Component	Value
C1	2.7 pF (0402)
C2, C4	0.57 pF[a]
C3	9.5 mm[b]
L1, L2, L3	11 nH (0402)
L4	9 mm[c]
C_T	STPTIC-27
C_M	STPTIC-27
L_{choke}	100 nH (0402, 0603)

[a] Capacitor made by microwave substrate (CuFlon).
[b] Length of the semi-rigid cable.
[c] Resonator loop diameter.

to the C_M served the purpose of increasing the matching region, similar to L3 that extends the tuning range. Two half-wave semi-rigid cables were used to separate the resonator head (see Fig. 4c) and the tuning and matching circuit, which should keep homogeneity of the static field and reduce the effect of the scan field on the circuit. The resonator head was made from nonmagnetic materials to avoid interaction with the main magnetic field. Choke inductors were inserted at many locations along the PCB to provide a stable ground for the PTICs and to reduce noise. The values for the capacitors and inductors are summarized in Table 1.

2.2. Digital signal processing in FPGA ICs

The RF signals from the resonator are filtered using a bandpass filter and digitized. The ADC samples signals at the frequency equal to the EPR frequency (around 1.2 GHz) multiplied by a factor of 4/11. This rate permits digital phase-sensitive detection (PSD) to retrieve the in-phase (I) and quadrature (Q) baseband components without multiplications and using a single ADC output [8,25]. Schematics of digital signal processing (DSP) that include automatic tuning and matching controls are shown in Fig. 5. Two FPGA ICs, which were programmed using Quartus II v14.1 (Intel Corp.) software, perform all DSP tasks.

2.2.1. Phase control of RF reflection signals

Operations of the digital PSD were necessary to acquire the I and Q reflection signals before the decimation of the data by a digital FIR low pass filter with a Blackman-Harris window, the number of taps 32 and decimation factor 2. The cutoff frequency of the filter was approximately 5 MHz, which gives the passband of 10 MHz. The intensities of the I and Q signals were then adjusted to be similar to each other by performing complex multiplication with $e^{-j\theta}$, where θ is the phase shift degree, which adjusted the phase of the RF reflected signal treated in the FPGA to be 45° or 225°.

Considering a 90° shift between EPR absorption and dispersion, down-converted signals $y(t)$ can be expressed by the following equation:

$$y(t) = I + jQ = \alpha(t)e^{i\frac{\pi}{4}} + \beta(t)e^{j\left(\frac{\pi}{4}+\frac{\pi}{2}\right)} = \frac{1}{\sqrt{2}}((\alpha(t) - \beta(t)) + j(\alpha(t) + \beta(t))) \quad (1)$$

where $\alpha(t)$ is sum of the reflection and the EPR dispersion component, $\beta(t)$ is the EPR absorption component. The subtraction of Q from I leaves the EPR absorption signal as indicated in Eq. (2). In contrast, the addition of I and Q deletes the EPR absorption signal, but does not eliminate the EPR dispersion signal overlapping in the reflection as indicated in Eq. (3).

$$Re[y] - Im[y] = -\sqrt{2}\beta \quad (2)$$

$$Re[y] + Im[y] = \sqrt{2}\alpha \quad (3)$$

The reason for the shift to 45° or 225° is to generate two control signals for the reflection reduction control, as mentioned in the next section. Phase shifts may not be exact. A value close to 45° can be found by searching for a phase position in the software at which the noise in the I – Q components reaches its minimum. At this value, the RF reflection is digitally cancelled as indicated in Eq. (2). The noise reduction occurs due to the cancellation of the phase noise contribution, which converted into the measured amplitude noise by the resonator [26].

The noise spectrum and RS-EPR signal are both monitored on a PC display. The phase of the I and Q signals is controlled from software using a time update function, which is equivalent to the accumulation time of the RS-EPR signal. Once the EPR digital console is switched on, this system can consistently maintain coherence in terms of its sub-sampling because the frequency-divided signals are generated from the single VCO and the signal acquisition is continuously running. Therefore, an RF phase shift to 45° or 225° applied in the FPGA can remain while the system is operating.

2.2.2. RS-EPR signal acquisition

The I – Q and I + Q signals are acquired and stored to a temporary RAM. Depending on the rapid scan field frequency, the sam-

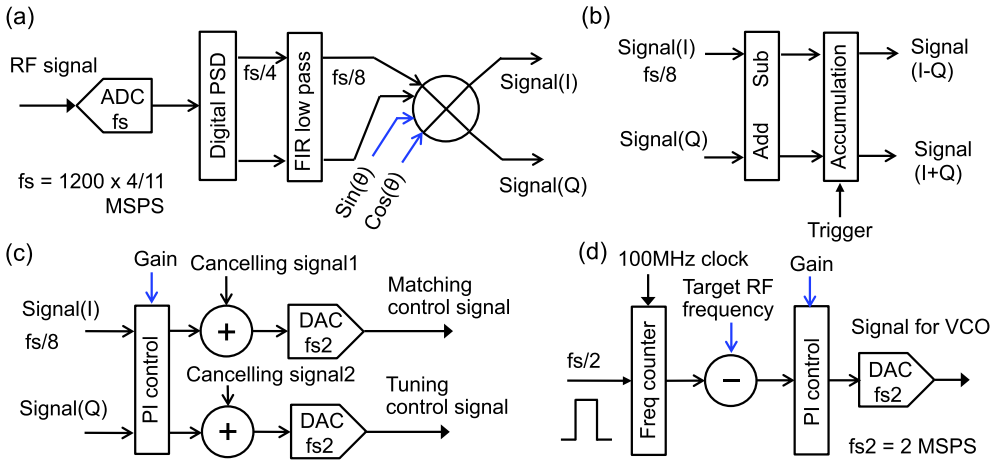

Fig. 5. Schematic diagram of the DSP at the FPGA ICs. (a) Generation of the baseband signals using digital PSD, (b) accumulation of the RS or FID signal, (c) generation of the matching and tuning control signals, (d) generation of the RF frequency control signal fed to the VCO tune port. Blue arrows express parameters updated from a PC. (For interpretation of the references to colour in this figure legend, the reader is referred to the web version of this article.)

pling frequency of the measured RS signals is selected to obtain a scan full period. The data length is 2560 points. EPR quadrature signals are acquired using post-processing in the PC. The PC controls the number of accumulation, start position of the accumulation, and a trigger position that define the first point of the acquired signals. The RS-EPR data are transferred to the PC from the RAM during the next accumulation of the RS-EPR signal so that no dead time occurred during data acquisition.

2.2.3. RF frequency control

The tuning signal for keeping the VCO frequency constant was generated with a proportional-integral (PI) negative feedback control. The frequency of the ADC clock which was derived from the VCO output was counted by comparing a 100 MHz reference frequency (SiT5002, SiTime Corp., USA). Then the difference between a target frequency and measured frequency was negatively feedbacked to generate the tuning signal.

2.2.4. Reflection reduction control

The reflection reduction control is based on the impedance control of the resonator which generates the reflection [7]. The generated reflection is combined with the leakage RF signal from the RF excitation and fed to the reception amplifier. To reduce the RF signal digitized by the ADC, we applied a PI negative feedback control. The down-converted baseband signals (I and Q) were used as two error signals for the PI control, which means the target of the control is no signal fed to the ADC. Two control signals are digitally generated from the error signals and then converted to be analog signals by two DAC ICs, as shown in Fig. 5.

If the RS-EPR signal bandwidth is higher than the feedback control bandwidth, the RS-EPR signal may be observed under the reflection reduction control. To eliminate the reflection arising from a magnetic field scan used to obtain the RS-EPR signal, cancelling signals were added to the control signals at the digital stage.

The voltage levels of tuning and matching control (TC and MC) signals were ranged from 0 to 22 V. These signals induced a bias voltage to the RF tunable capacitors in the tuning and matching circuit to adjust the impedance of the resonator. Two CR filters with a cut-off frequency of 1.6 kHz were used to smooth the feedback signals and to attenuate the RF leaks from the matching and tuning circuit. Two separate feedback signals were required for the matching and tuning of the resonator. Therefore, a phase shift of either 45° or 225° was applied to the reflected signals treated in the FPGA.

2.2.5. Magnetic field scan control

Magnetic field scan control signal was generated with integral feedback control as shown in Fig. 6. The phase and amplitude of the sinusoidal control signal were determined based on the measurement of the current through the coil. The scan control signal is generated with an NCO1, which phase increment value is a user-defined parameter. The measured analog signal is digitized with the serial ADC in the console, then the in-phase and quadrature components of the baseband signal are obtained using the digital PSD. For the PSD, a reference clock was generated with an NCO5 which frequency was 4 times higher than the frequency of the NCO1. One of the components is integrated and then used for the phase control signal for the NCO1 to make this component become zero. The other component is subtracted with the target value for controlling the amplitude of the field scan, then the difference was integrated and used for the digital gain applied to the output of the NCO1. An NCO2 was used to generate a trigger signal for the accumulation of the RS-EPR signal. The frequency of the NCO2 was the same as that of the NCO1. The phase of the NCO2 was a user-defined parameter to shift the position to start accumulation within the period of the field scan.

2.2.6. Background signal cancellation control

Sinusoidal background signals are often observed in RS-EPR experiments [27]. This signal is the result of coupling between the magnetic field scan and RF electronics. We observed a change of the background intensity that was dependent on the location of the cables for tuning and matching control signals. A method of digital background cancellation was implemented. This method subtracts a sinusoidal background component before digitizing RS-EPR signals by manipulating RF reflection. Amplitude and phase of the waveform are software-controlled. The NCO3 and the NCO4 are used for this purpose as shown in Fig. 6. The background cancelling signals are added to the feedback signals for tuning and matching controls before converting to the analog signals as shown in Fig. 5.

2.3. Conversion of RS-EPR signal to slow scan EPR spectrum

Most of the control and DSP for the RS-EPR were carried on the FPGA ICs except the conversion of the RS-EPR to slow scan EPR spectrum using a deconvolution method code [15]. The deconvolution algorithm was originally developed in MATLAB code. Since our digital spectrometer is controlled using LabVIEW code, it was convenient to rewrite the deconvolution algorithm in this language.

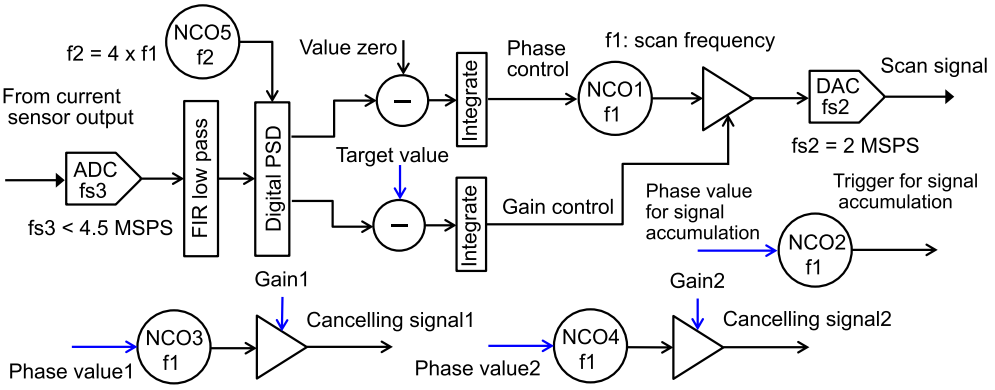

Fig. 6. Schematic diagram of the DSP for amplitude and phase control of the scan field. Two cancelling signals to eliminate field scan effect to the background of RS-EPR signals were also shown, which required manual adjustment. Blue arrows express parameters updated from a PC. (For interpretation of the references to colour in this figure legend, the reader is referred to the web version of this article.)

The LabVIEW-based deconvolution program is used for scan field calibration, background compensation, and real-time displaying of the measured EPR spectra. To increase the resolution of the converted spectrum, the FFT interpolation function was added. For estimation of the half-magnitude linewidth of the spectrum, the nonlinear curve fitting with the Lorentz function based on the Levenberg-Marquardt method was included in the program. Complete data processing is accomplished before the next dataset is sent from the FPGA to the PC. The scan field amplitude was calibrated based on the measured EPR line position shift as a result of the RF frequency change.

2.4. Evaluation of RS-EPR digital console

RF frequency, scan field, and reflection reduction controls operate using the negative feedback loop that runs on the FPGA IC. These controls were evaluated with a sample of lithium octa-n-butoxy 2,3-naphthalocyanine (LiNc-BuO) microcrystals and tempone-d16 which show narrow linewidth EPR spectra. LiNc-BuO is used in EPR oximetry, including clinical applications as an oxygen sensitive core of the OxyChip [28]. The sample (approximately 1 mm height) was located in a 1 mm o.d. Teflon tube and sealed by heat. Then, the Teflon tube was put into another plastic tube through which nitrogen gas was pumped from a liquid nitrogen tank. Oxygen gas surrounding the sample was replaced by nitrogen gas through a wall of the Teflon tube to give a narrow linewidth EPR spectrum. By changing the number of accumulations, the linewidth broadening was measured. 0.83 mM tempone-d16 aqueous solution 50 μL (ambient oxygen pressure) was prepared and placed in a 4 mm o.d. plastic tube which was used to evaluate the background cancelling method using a large field scan amplitude of 3 mT that amplified the background intensity.

The stability of the RF frequency, which was measured using a spectrum analyzer (N9340B, Keysight Technologies, USA), was less than 5 kHz for the prescaler-based RF generator. This amount of fluctuation may produce up to 0.18 μT EPR line broadening at 1.2 GHz, a negligible spectral distortion for the majority of spin probes.

Three major noise sources that contribute to EPR spectra can be distinguished: (i) digital console noise; (ii) noise in the RF excitation signal, and (iii) ambient RF noise. The latter is the most challenging source to eliminate. It often helps to detune the EPR frequency from a pickup signal generated by an external device, such as a mobile network. To evaluate the noise of the console at 1.2 GHz, the resonator which connected with the circulator was replaced with the 50 Ω terminator, and the input of the circulator was also terminated with 50 Ω. As a result, the noise due to the system itself was measured. The noise contribution of the RF generator was investigated by changing the power of the CW excitation. Noise spectral density plots were generated from the 100 times average of the fast Fourier transformed (FFT) of the single scan obtained by the digital console. These noise floor values were calibrated with the spectrum analyzer (N9340B) considering the gain of the analog front-end. All of the noise measurement was done without an RF shielding box or a shielding room.

3. Results and discussion

3.1. Resonator with tuning and matching circuit

An electrically tunable single loop-gap resonator was made for 1.2 GHz operation. This is to confirm whether the developed RS-EPR console is working properly for RS-EPR detection, reflection reduction, and cancellation of the background due to the field scan. The quality factor of the resonator was estimated from the reflection coefficient measurement using a network analyzer (E5061A, Keysight Technologies) at different conditions as shown in Fig. 7. The bias voltages applied to the RF tunable capacitors were different for each case. The rough adjustment of the resonant frequency to 1.2 GHz was made by changing the length of the loop. The loaded Q varied from 15 to 120 depending on the samples. Fig. 8 shows the intensities of the free induction decay (FID) from the deoxygenated LiNc-BuO as a function of the power of the excitation pulse. The tiny sample was placed at the center of the loop. The data were fitted by using a damped sine curve function. From the result, the power of

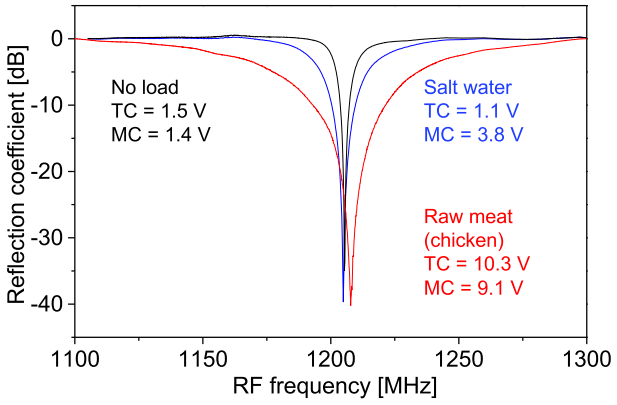

Fig. 7. Reflection coefficient curves of the 1.2 GHz single loop-gap resonator with different loads.

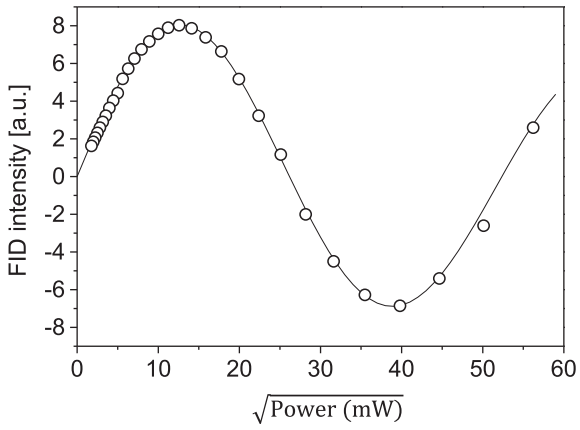

Fig. 8. FID intensities from the LiNc-BuO probe plotted as a function of the power inserted into the circulator. These signals were observed with the following parameters; RF frequency 1.207 GHz, number of accumulations 1000, Q of the resonator around 120. The line was the result of the fitting with a damped sine function.

the 90-degree pulse was around 0.16 W. Considering the pulse width of 220 ns, the generation efficiency of the RF field was calculated to be around 0.10 mT/W$^{0.5}$, which was similar range reported for the other electrically tunable single loop-gap resonator using varactor diodes as a tunable capacitor [29].

Fig. 9a shows the result of the TC and MC signals plotted as a function of the RF frequency for the resonator with/without salted water in the resonator loop. The TC and MC signals were obtained using the feedback control working while the frequency of the excitation wave to the resonator was swept from 1195 to 1220 MHz. As the result, the tunable frequency region was estimated to be in the range from 15 to 20 MHz. The capacitances of the PTICs were estimated using the relationship between the bias voltage and capacitance shown in the manufacturer datasheet. The large change of the capacitance observed for the tuning PTIC was as expected since the RF frequency was swept and the resonant frequency was followed. The small change of the capacitance for the matching PTIC means that the loss of the resonator kept almost the same with the frequency sweep since the load of the resonator was the same as well.

3.2. Background signal cancellation

A sinusoidal background signal is often observed in RS-EPR experiments, which is the result of a coupling between the magnetic field scan and RF circuits [30,31]. This coupling gets stronger as the RF and scan amplitudes increase. We observed that the location of the cables and the cutoff frequency of the low pass filter used for tuning and matching controls affected the phase and amplitude of the background signal, which indicated that the scan field interfered with the bias voltage of the PTIC. Changes in the total resonator impedance cause RF reflections, resulting in a background signal.

Fig. 10 shows experimental data measured using field scans with the amplitude of 3 mT and the frequency of 33.9 kHz. The signals were averaged 2000 times. The reflection reduction control was operational. An aqueous solution of tempone-d16 (0.83 mM, 50 uL) was used to observe RS-EPR signals. Fig. 10 shows that the background signal is comparable in amplitude (μV range) with the RS-EPR signal. The background spectrum is dominated by the first harmonic of the scan frequency, which simplifies its removal as shown in Fig. 10. A quadrature signal was generated to compensate both in-phase and out-of-phase contributions of the first harmonic interference signal. This procedure was successfully implemented to acquire undistorted RS signals (see Fig. 10b). The overcompensated signal measured in the absence of the scanning magnetic field is shown in Fig. 10c. This signal, which is 180° out-of-phase with respect to the background signal, cancels the latter out.

The phases and amplitude for the cancelling signals are adjusted manually in the current design. However, automatic control using the FPGA IC may be possible. Toward this goal, phase sensitive detection of the bias voltage at the position of the PTIC can be feedbacked to the phase and amplitude of the cancelling signal if the background signal primary is the result of PTIC capacitance fluctuations.

3.3. RS and pulsed EPR measurements at 1.2 GHz

RS and pulsed EPR measurements were performed and compared to evaluate the digital system performance. Fig. 11a shows RS-EPR signals measured using LiNc-BuO probes at 1.205 GHz. The scan field parameters were as follows: frequency was 15 kHz, peak-to-peak amplitude was 0.159 mT, RF incident power at the input port of the circulator was −0.6 dBm (0.9 mW) and 5.3 dBm (3.4 mW). Sampling frequency 37.5 MSPS, number of accumulations 100 and passband of the digital filter 10 MHz were used in the experiments. Fig. 11b shows FID signals from the same LiNc-BuO sample. The parameters were as follows: RF excitation power at the input port of the circulator was 33.2 dBm (2.1 W), a 90°-pulse had a duration of 220 ns, the number of accumulations was 100 and passband of the digital filter was 10 MHz. The Q factor

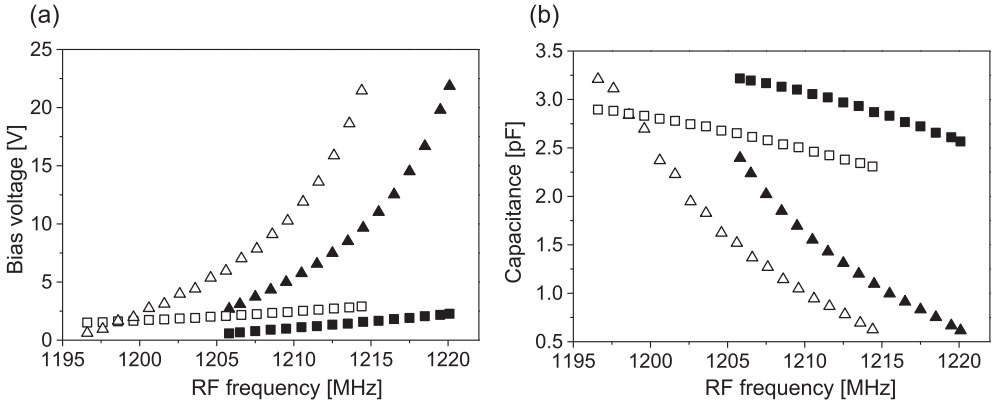

Fig. 9. (a) Bias voltages induced to the tunable capacitors (PTICs) for matching (square mark) and tuning (triangle mark) of the 1.2 GHz resonator as a function of the RF frequency. (b) The capacitances of the PTICs converted from the relationship between bias voltage and capacitance reported in the manufactured datasheet. Closed marks express the results from the resonator without sample, while blank marks express the results from the resonator with the tube containing salt water.

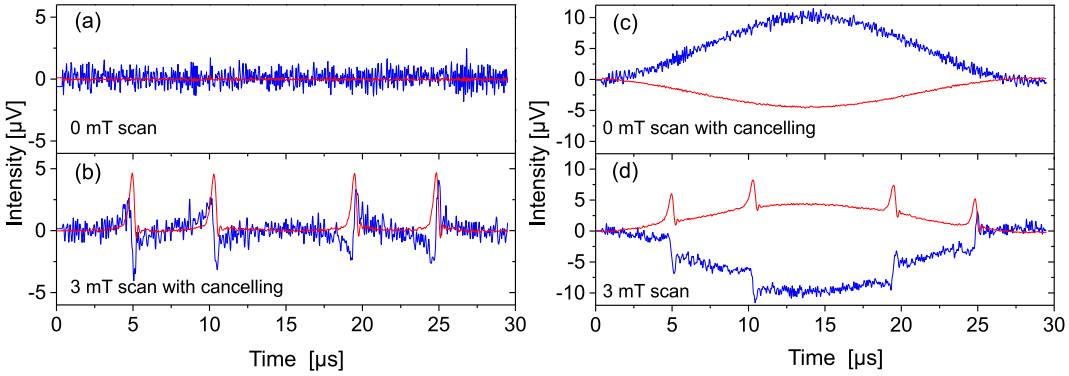

Fig. 10. Quadrature components of the background signals under no field scan (a), 3 mT sinusoidal field scan with background cancelling (b), no field scan with background cancelling (c), 3 mT sinusoidal field scan (d). These signals were observed with the following parameters; scan frequency 33.9 kHz, RF frequency 1.205 GHz, RF power 8.2 dBm, number of accumulations 2000, Q of the resonator around 120. As an EPR reference, tempone-d16 in aqueous solution (0.83 mM, 50 μL) was inserted in the resonator loop.

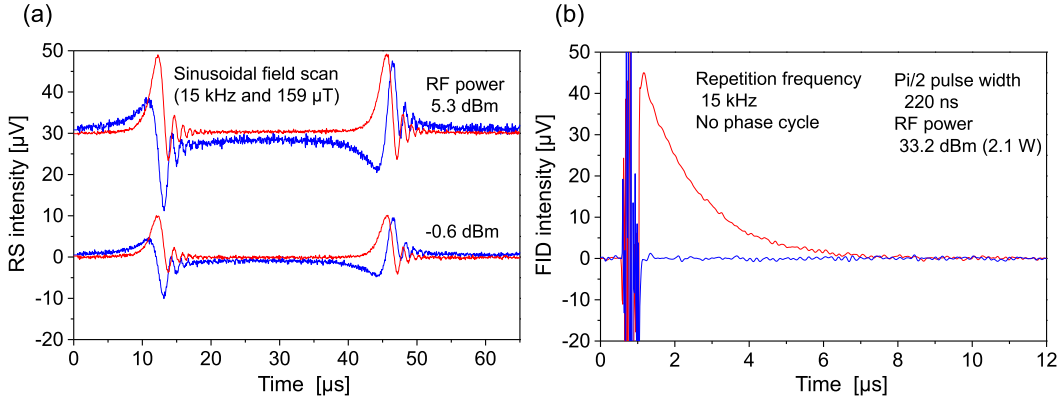

Fig. 11. Quadrature signals of 1.2 GHz RS-EPR (a) and FID (b) from the LiNc-BuO probe with signal accumulation 100 and passband of the digital filter 10 MHz. Red and blue lines express out-of-phase and in-phase components, respectively. The Q of the resonator decreased to be around 45 by inserting the salt water in the resonator loop. The sample was placed 3 mm away from the loop. (For interpretation of the references to colour in this figure legend, the reader is referred to the web version of this article.)

of the resonator was reduced to 45 by inserting a tube containing saturated salt water into the resonator. This low Q value emulates *in-vivo* conditions and increases the excitation/detection bandwidth. The LiNc-BuO sample was placed at around 3 mm lower from the resonator loop. The final FID signal was obtained by subtraction of the off-resonance background. The early portion of the signal was distorted because of the reduction of the RF excitation signal and its ringing due to the limiter PIN diode and the overflow of the signal accumulation in the FPGA. Spin-spin relaxation time T_2 was 1.47 ± 0.01 μs that was estimated from the exponential fitting of the measured FID signal. The noise of the in-phase component was lower compared to the RS-EPR measurements due to the absence of RF excitation during the signal detection.

The converted slow scan EPR spectra were shown in Fig. 12a, while the FFT spectrum of the FID signal was shown in Fig. 12b. The half-magnitude linewidths estimated for the RS-EPR varied with the RF excitation power as shown in Table 2. The error was defined as a standard deviation (SD) calculated from consecutive 150 sets of accumulated scans. The increase of the linewidth depended on the RF power for the RS-EPR was owing to the saturation of the signal. However, the values at the power level below 5.3 dBm was less than 5% difference from the one estimated from the FID. This indicated that the RS-EPR system and deconvolution algorithm are working correctly. The function of the signal accumulation was checked with different accumulation number 10, 100, 1000, and 10,000. Those accumulation times were corresponding to 0.66 ms, 6.6 ms, 66 ms, and 662 ms, respectively. The results were also summarized in Table 2. The linewidths did not change with the number of accumulations, which indicated that the scan field control and frequency control were sufficiently stable within 1 s required for the EPR signal acquisition.

3.4. Noise of RS and pulsed EPR system

The noise spectral densities of the receiver were measured using the following conditions: automatic reflection reduction control in operation, no scanning field, and the RF power of 16.6 dBm, 11.1 dBm, 5.0 dBm. To obtain reference measurements, the noise spectral density from the circulator whose ports for RF excitation and to the resonator were terminated with the 50 Ω resistors was measured. The results are shown in Fig. 13. The y-axis corresponds to the digitally filtered intensity that is mostly below the thermal noise level of −174 dBm/Hz at room temperature. The intensities of the observed raw data were above the thermal noise level.

The noise spectrum of the 50 ohms terminated system, which was expressed in a black line in the figure, was affected by the FIR lowpass filter which had the passband of around 10 MHz. From the noise level, thermal noise of the RF components in front of the LNA was the main cause of the noise floor without the resonator under no RF excitation. A spike peak at 5.48 MHz was an internal noise due to the difference of the carrier frequency (1.205 GHz) and the 17th harmonic (71.2 MHz) of the serial ADC clock signal. There were some spike peaks observed after connecting the resonator. These intensities did not depend on the power of the RF excitation, which indicates that these are probably external noise

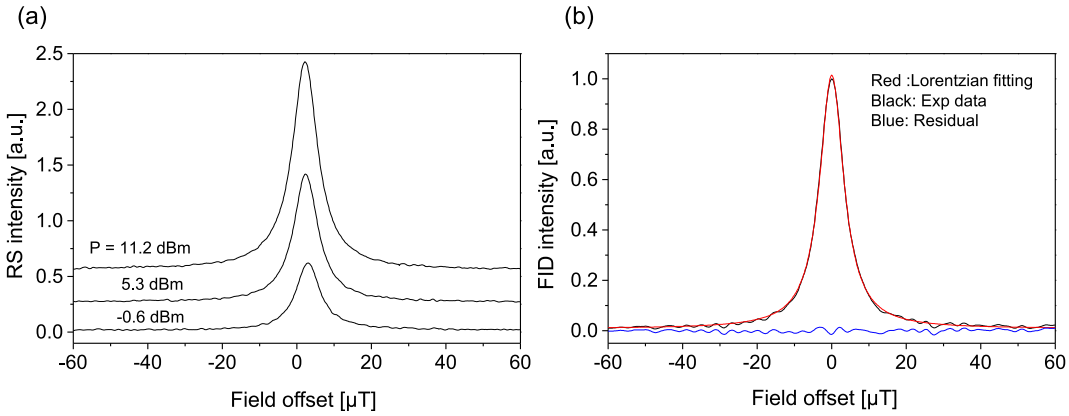

Fig. 12. Slow scan absorption LiNc-BuO spectra converted from the RS-EPR signal (a) and the FFT spectrum (b) from the FID signal shown in Fig. 11. A line (blue) obtained by subtracting a fitting curve (red) from the spectrum is also shown in (b). (For interpretation of the references to colour in this figure legend, the reader is referred to the web version of this article.)

Table 2
The linewidths estimated from LiNc-BuO RS-EPR spectra measured with various RF power and number of accumulations. As a reference, the results from the FID measurements were added in the table.

Mode	Power (dBm)	Accumulation	Linewidth (μT)	SD[a] (μT)
RS	14.2	100	9.12	0.04
RS	11.2	100	8.50	0.03
RS	8.2	100	8.20	0.03
RS	5.3	100	8.05	0.03
RS	2.6	100	7.97	0.04
RS	−0.6	100	7.91	0.05
RS	−3.8	100	7.88	0.07
RS	−5.9	100	7.88	0.09
RS	5.3	10	8.09	0.10
RS	5.3	100	8.09	0.03
RS	5.3	1000	8.08	0.01
RS	5.3	10,000	8.09	0.01
FID	33.2	100	7.75	0.05
FID	33.2	1000	7.74	0.02

[a] Standard deviation (SD) of the linewidth.

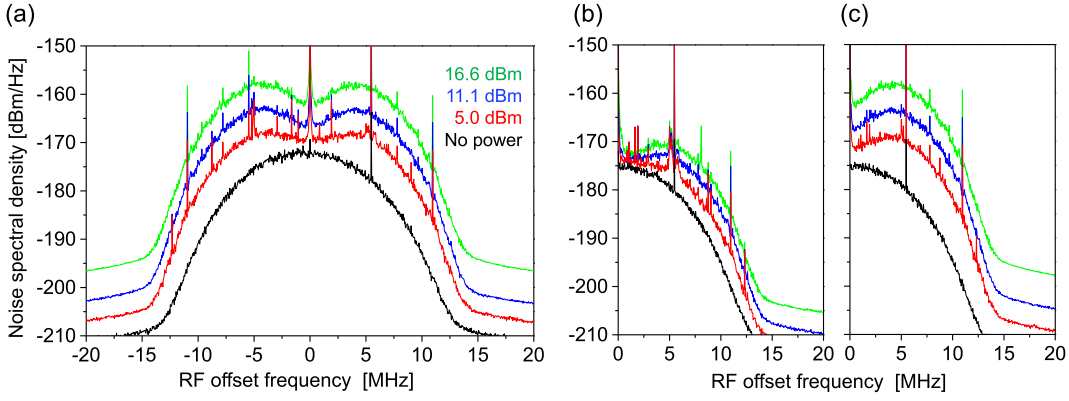

Fig. 13. Noise spectral densities of the received signals with different RF excitation power with the LGR under the refection reduction control (a), qudratrue phase noise components corresponding to out-of-phase (b) and in-phase (c) contributions. As a reference, the noise spectral density (a black line) obtained using 50 Ω termination of the circulator without the reflection control was also shown.

captured from the resonator. However, these peaks are often averaged out using signal accumulation because they are not synchronized with the digital system clock. The noise reduction shown in Fig. 13 in the vicinity of the carrier frequency is the result of the limited resonator bandwidth. The spike peaks observed at the center were due to the combination of the leaked RF excitation signal and the reflection signal to the reception, which should be suppressed due to the reflection reduction control. When the power of the RF excitation was 16.6 dBm, the attenuated RF power fed to the reception was −80 dBm. Therefore, the difference of 100 dB was suppressed, which is well below the isolation of the circulator (approximately 20 dB).

The difference of the noise floor for out-of-phase and in-phase components was due to the noise from the RF generator since the noise in the in-phase component linearly depended on the power of the RF excitation. An RF generator with better phase noise

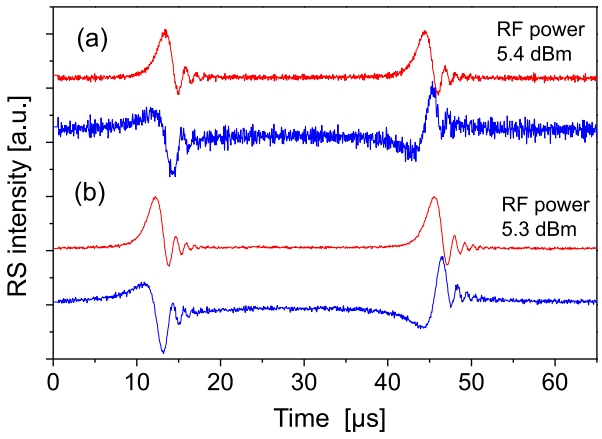

Fig. 14. RS-EPR signals from the LiNc-BuO probe measured with the DDS-based RF generator (a) and the prescaler-based generator (b), both of which are described in Fig. 2. The sample and receiver circuit were the same, while the CW excitation power was adjusted to be similar using the attenuators.

property and floor noise can be used to reduce this noise contribution. Several RF generators were tested as shown in Fig. 14. Similar results were reported in the previous work [7]. The typical phase noise at 100 kHz offset of the VCO used for the prescaler-based RF generator was −115 dBm/Hz at the carrier frequency of 9.6 GHz. Then, a frequency division factor of 8 decrease phase noise 18 dB theoretically. Therefore, the estimated phase noise for 1.2 GHz at 100 kHz offset is −133 dBm/Hz. The RS-EPR signals are measured with the presence of the CW RF excitation, so that the phase noise in the RF excitation degrades the EPR in-phase component since the phase is same as that of the RF excitation. Ideally, the contribution of the phase noise of the RF excitation does not impact on the out-of-phase component of the RS-EPR signal. However, the noise floor in the out-of-phase component was also moderately increased. The possible explanation is an additive phase noise of the RF components which deteriorate the phase noise coherence between the RF excitation signal and digitalization of the signal with the ADC. In addition, inadequate selection of the bandpass filter may contribute to noise increase due to aliasing. The rough estimation of the noise figure of the digital console including the analog front-end was 5 dB for out-of-phase component at the RF excitation power of 16.6 dBm, offset of 2 MHz and the resonator Q of around 45.

4. Conclusions

We have developed an L-band RS-EPR digital console for *in-vivo* applications. This console has a number of FPGA-based digital controls, including for magnetic field scan, reflection reduction, RF excitation frequency, and background cancellation. The automatic reflection reduction control applied to an electrically tunable single loop-gap resonator provided stable reflection suppression over a wide range of RF frequencies. The developed digital console was shown to be easily adjusted for different types of loads, including lossy biological objects. Experimental comparison of RS spectra and pulsed EPR measurements was performed. Towards this goal, a simple pulsed EPR option was integrated into the digital system using the RF generator based on 3.5 GSPS DDS ICs. The RS and pulsed spectra of the LiNc-BuO probe had a similar linewidth. This comparison results indicated that the RS-EPR measurements were accurate and not affected by the automatic reflection reduction control. In future studies, this system will be used in *in-vivo* EPR applications, where animal motion often generates excessive RF reflection.

Acknowledgments

The authors thank Mr. K. Tsuji (Osaka University) for fabrication of the field scan coils. The help of Dr. Andrey Bobko and Oxana Tseytlin in preparation for the sample is greatly appreciated. This work was supported by grants from the Japan Society for the Promotion of Science (16K14275 and 18K04164 to H.S.). The support of this work for the development of rapid scan EPR software by NIH R21 EB022775 (M.T.) is gratefully acknowledged.

References

[1] J. Forrer, H. Schmutz, R. Tschaggelar, A. Schweiger, Direct EPR detection of transient and continuous wave signals at 2.5 GHz, J. Magn. Reson. 166 (2004) 246–251, https://doi.org/10.1016/j.jmr.2003.10.022.
[2] J.S. Hyde, T.G. Camenisch, J.J. Ratke, R.A. Strangeway, W. Froncisz, Digital detection by time-locked sampling in EPR, Biol. Magn. Reson. 24 (2005) 199–222, https://doi.org/10.1007/0-306-48533-8_7.
[3] R.H. Pursley, G. Salem, T.J. Pohida, N. Devasahayam, S. Subramanian, M.C. Krishna, Direct detection and time-locked subsampling applied to pulsed electron paramagnetic resonance imaging Direct detection and time-locked subsampling applied to pulsed electron paramagnetic resonance imaging, Rev. Sci. Instrum. 76 (2005) 053709, https://doi.org/10.1063/1.1903163.
[4] R. Ahmad, S. Som, E. Kesselring, P. Kuppusamy, J.L. Zweier, L.C. Potter, Digital detection and processing of multiple quadrature harmonics for EPR spectroscopy, J. Magn. Reson. 207 (2010) 322–331, https://doi.org/10.1016/j.jmr.2010.09.016.
[5] M. Tseitlin, R.W. Quine, G.A. Rinard, S.S. Eaton, G.R. Eaton, Digital EPR with an arbitrary waveform generator and direct detection at the carrier frequency, J. Magn. Reson. 213 (2011) 119–125, https://doi.org/10.1016/j.jmr.2011.09.024.
[6] M. Tseitlin, Z. Yu, R.W. Quine, G.A. Rinard, S.S. Eaton, G.R. Eaton, Digitally generated excitation and near-baseband quadrature detection of rapid scan EPR signals, J. Magn. Reson. 249 (2014) 126–134, https://doi.org/10.1016/j.jmr.2014.10.011.
[7] H. Sato-Akaba, M.C. Emoto, H. Hirata, H.G. Fujii, Design and testing of a 750 MHz CW-EPR digital console for small animal imaging, J. Magn. Reson. 284 (2017) 48–58, https://doi.org/10.1016/j.jmr.2017.09.008.
[8] R.G. Vaughan, N.L. Scott, D.R. White, The theory of bandpass sampling, IEEE Trans. Signal Process. 39 (1991) 1973–1984, https://doi.org/10.1109/78.134430.
[9] M.C. Emoto, H. Sato-Akaba, Y. Matsuoka, K. Yamada, H.G. Fujii, Non-invasive mapping of glutathione levels in mouse brains by in vivo electron paramagnetic resonance (EPR) imaging: applied to a kindling mouse model, Neurosci. Lett. 690 (2019) 6–10, https://doi.org/10.1016/J.NEULET.2018.10.001.
[10] H. Fujii, M. Emoto, H. Sato-Akaba, Brain redox imaging using in vivo electron paramagnetic resonance imaging and nitroxide imaging probes, 2019. doi: 10.3390/magnetochemistry5010011.
[11] J.W. Stoner, D. Szymanski, S.S. Eaton, R.W. Quine, G.A. Rinard, G.R. Eaton, Direct-detected rapid-scan EPR at 250 MHz, J. Magn. Reson. 170 (2004) 127–135, https://doi.org/10.1016/J.JMR.2004.06.008.
[12] S. Subramanian, J.W. Koscielniak, N. Devasahayam, R.H. Pursley, T.J. Pohida, M. C. Krishna, A new strategy for fast radiofrequency CW EPR imaging: direct detection with rapid scan and rotating gradients, J. Magn. Reson. 186 (2007) 212–219, https://doi.org/10.1016/J.JMR.2007.01.023.
[13] T. Czechowski, W. Chlewicki, M. Baranowski, K. Jurga, P. Szczepanik, P. Szulc, K. Tadyszak, P. Kedzia, M. Szostak, P. Malinowski, S. Wosinski, W. Prukala, J. Jurga, Two-dimensional EPR imaging with the rapid scan and rotated magnetic field gradient, J. Magn. Reson. 248 (2014) 126–130, https://doi.org/10.1016/J.JMR.2014.09.022.
[14] S.S. Eaton, Y. Shi, L. Woodcock, L.A. Buchanan, J. McPeak, R.W. Quine, G.A. Rinard, B. Epel, H.J. Halpern, G.R. Eaton, Rapid-scan EPR imaging, J. Magn. Reson. 280 (2017) 140–148, https://doi.org/10.1016/j.jmr.2017.02.013.
[15] M. Tseytlin, Full cycle rapid scan EPR deconvolution algorithm, J. Magn. Reson. 281 (2017) 272–278, https://doi.org/10.1016/j.jmr.2017.06.008.
[16] G.A. Rinard, R.W. Quine, J.R. Biller, G.R. Eaton, A wire crossed-loop-resonator for rapid scan EPR, Concepts Magn. Reson. Part B. Magn. Reson. Eng. 37B (2010) 86–91, https://doi.org/10.1002/cmr.b.20161.
[17] B. Epel, S.V. Sundramoorthy, M. Krzykawska-Serda, M.C. Maggio, M. Tseytlin, G.R. Eaton, S.S. Eaton, G.M. Rosen, J.P.Y. Kao, H.J. Halpern, Imaging thiol redox status in murine tumors in vivo with rapid-scan electron paramagnetic resonance, J. Magn. Reson. 276 (2017) 31–36, https://doi.org/10.1016/j.jmr.2016.12.015.
[18] L.A. Buchanan, L.B. Woodcock, G.A. Rinard, R.W. Quine, Y. Shi, S.S. Eaton, G.R. Eaton, 250 MHz rapid scan cross loop resonator, Appl. Magn. Reson. 50 (2019) 333–345, https://doi.org/10.1007/s00723-018-1078-y.
[19] R.P. Pandian, N.L. Parinandi, G. Ilangovan, J.L. Zweier, P. Kuppusamy, Novel particulate spin probe for targeted determination of oxygen in cells and tissues, Free Radic. Biol. Med. 35 (2003) 1138–1148, https://doi.org/10.1016/S0891-5849(03)00496-9.
[20] J. Frank, D. Gündel, S. Drescher, O. Thews, K. Mäder, Injectable LiNc-BuO loaded microspheres as in vivo EPR oxygen sensors after co-implantation with tumor

cells, Free Radic. Biol. Med. 89 (2015) 741–749, https://doi.org/10.1016/J.FREERADBIOMED.2015.10.401.
[21] H. Hirata, T. Walczak, H.M. Swartz, Electronically tunable surface-coil-type resonator for L-band EPR spectroscopy, J. Magn. Reson. 142 (2000) 159–167, https://doi.org/10.1006/jmre.1999.1927.
[22] H. Yokoyama, T. Sato, T. Ogata, H. Ohya, H. Kamada, Automatic coupling control of a loop-gap resonator by a variable capacitor attached coupling coil for EPR measurements at 650 MHz, J. Magn. Reson. 149 (2001) 29–35, https://doi.org/10.1006/jmre.2000.2268.
[23] G.L. He, S. Petryakov, A. Samouilov, M. Chzhan, P. Kuppusamy, J.L. Zweier, Development of a resonator with automatic tuning and coupling capability to minimize sample motion noise for in vivo EPR spectroscopy, J. Magn. Reson. 149 (2001) 218–227, https://doi.org/10.1006/jmre.2001.2293.
[24] H. Sato-Akaba, H. Fujii, H. Hirata, Improvement of temporal resolution for three-dimensional continuous-wave electron paramagnetic resonance imaging, Rev. Sci. Instrum. 79 (2008).
[25] J.S. Hyde, H.S. Mchaourab, T.G. Camenisch, J.J. Ratke, R.W. Cox, J.S. Hyde, H.S. Mchaourab, T.G. Camenisch, J.J. Ratke, R.W. Cox, W. Froncisz, Electron paramagnetic resonance detection by time-locked subsampling, Rev. Sci. Instrum. 69 (1998) 2622–2628, https://doi.org/10.1063/1.1148989.
[26] G.A. Rinard, R.W. Quine, B.T. Ghim, S.S. Eaton, G.R. Eaton, Easily tunable crossed-loop (Bimodal) EPR resonator, J. Magn. Reson. Ser. A 122 (1996) 50–57, https://doi.org/10.1006/jmra.1996.0173.
[27] M. Tseitlin, D.G. Mitchell, S.S. Eaton, G.R. Eaton, Corrections for sinusoidal background and non-orthogonality of signal channels in sinusoidal rapid magnetic field scans, J. Magn. Reson. 223 (2012) 80–84, https://doi.org/10.1016/j.jmr.2012.07.023.
[28] G. Meenakshisundaram, E. Eteshola, R.P. Pandian, A. Bratasz, S.C. Lee, P. Kuppusamy, Fabrication and physical evaluation of a polymer-encapsulated paramagnetic probe for biomedical oximetry, Biomed. Microdev. 11 (2009) 773–782, https://doi.org/10.1007/s10544-009-9292-x.
[29] H. Hirata, T. Walczak, H. Swartz, Characteristics of an electronically tunable surface-coil-type resonator for L-band electron paramagnetic resonance spectroscopy, 2001. doi: 10.1063/1.1372665.
[30] M. Tseitlin, T. Czechowski, R.W. Quine, S.S. Eaton, G.R. Eaton, Background removal procedure for rapid scan EPR, J. Magn. Reson. 196 (2009) 48–53, https://doi.org/10.1016/j.jmr.2008.10.012.
[31] L.A. Buchanan, L.B. Woodcock, R.W. Quine, G.A. Rinard, S.S. Eaton, G.R. Eaton, Background correction in rapid scan EPR spectroscopy, J. Magn. Reson. 293 (2018) 1–8, https://doi.org/10.1016/j.jmr.2018.05.010.